The Astronomical Journal, 159:50 (14pp), 2020 February https://doi.org/10.3847/1538-3881/ab607e

Identifying Multiple Populations in M71 Using CN

Jeffrey M. Gerber, Eileen D. Friel, and Enrico Vesperini
Department of Astronomy, Indiana University Bloomington, Swain West 319, 727 East 3rd Street, Bloomington, IN 47405-7105, USA
Received 2019 April 25; revised 2019 November 22; accepted 2019 November 23; published 2020 January 13

Abstract

We have observed the CN features at ∼3800 and 4120 Å as well as the CH band at ∼4300 Å for 145 evolved stars in the Galactic globular cluster M71 using the multi-object spectrograph, Hydra, on the Wisconsin-Indiana-Yale-NOAO-3.5 m telescope. We use these measurements to create two δCN indices finding that both distributions are best fit by two populations: a CN-enhanced and CN-normal. We find that 42% ± 4% of the red giant branch stars in our sample are CN-enhanced. The percentage of CN-enhanced is 40% ± 13% for the asymptotic giant branch and 33% ± 9% for the horizontal-branch stars (HB stars), which suggests there are no missing second generation stars at these stages of stellar evolution. The two generations also separate in magnitude and color on the HB, which allows us to find the difference in He abundance between the two populations by fitting appropriate zero-age horizontal branches. The broad range of distances from the cluster's center covered by our sample allows us to study the dependence of the ratio of the number of first to second population stars on the distance from the cluster's center, and we find that this ratio does not vary radially and that the two populations are spatially mixed. Finally, we compare our identification of multiple populations with the classification based on the Na–O anti-correlation and the *Hubble Space Telescope* UV photometry, and we find good agreement with both methods.

Unified Astronomy Thesaurus concepts: Globular star clusters (656); Stellar astronomy (1583); Spectroscopy (1558)

Supporting material: machine-readable table

1. Introduction

Once thought to be simple stellar populations, globular clusters (GCs) are now known to have much more complicated abundance patterns, indicating the presence of multiple stellar populations. Studies of light elements have now revealed anti-correlations in C–N, Na–O, and Mg–Al indicative of multiple epochs of star formation taking place within GCs (see, e.g., Kraft 1994; Gratton et al. 2012, and references therein). Photometric surveys searching for multiple populations in Galactic GCs using *Hubble Space Telescope* (*HST*) UV photometry have also found that these multiple populations exist in every Galactic GC observed (see, e.g., Piotto et al. 2015; Milone et al. 2017). These studies show that GCs can no longer be considered as simple stellar populations.

Multiple theories have been proposed to explain the formation of these multiple populations, and the progenitors that would have supplied the material to pollute the intracluster medium with the abundance patterns observed (see, e.g., Gratton et al. 2012, and references therein). The possible sources of processed gas suggested in the literature include massive asymptotic giant branch (AGB) stars (see, e.g., Ventura et al. 2001; D'Ercole et al. 2008, 2012; D'Antona et al. 2016), fast-rotating massive stars (Prantzos & Charbonnel 2006; Decressin et al. 2007b), massive binary stars (de Mink et al. 2009), massive stars (Elmegreen 2017), and super-massive stars (Denissenkov & Hartwick 2014; Gieles et al. 2018). However, no consensus has been reached on any model for the formation history of multiple populations, and most questions concerning the origin of the observed abundance patterns are still unanswered.

The light element abundance patterns of the evolved, red giant branch (RGB) stars in GCs are complicated even further by a secondary mixing phenomenon that brings CN(O)-cycle material from the H-burning layer up to the surface of these stars. Secondary mixing begins in low mass stars (0.5–2.0 $M_{\odot}$) once they have passed the evolutionary stutter of the luminosity function bump. After passing this point on the RGB, the influx of CN(O)-cycle material being brought to the surface causes the surface abundance of carbon to decrease while nitrogen increases. Multiple theories to explain this non-canonical mixing have been presented and include thermohaline mixing, rotation, and magnetic fields, with thermohaline mixing often being favored (see, e.g., Kippenhahn et al. 1980; Eggleton et al. 2006; Charbonnel & Zahn 2007; Denissenkov & Merryfield 2011; Traxler et al. 2011; Wachlin et al. 2011; Brown et al. 2013; Henkel et al. 2017, and references therein).

Due to these complications, large sample sizes (∼100 or more) are needed to study the light element abundance patterns of evolved stars in GCs. Especially when studying carbon and nitrogen, large numbers are needed to separate the effects of multiple populations and secondary mixing in causing inhomogeneities in abundance patterns; both effects cause an anti-correlation in carbon and nitrogen since both involve some form of "pollution" from CN(O)-cycled material.

In this paper, we continue our previous work on multiple populations in GCs (Gerber et al. 2018, hereafter referred to as "G18") with a sample size of approximately 150 stars in M71; a relatively high metallicity Galactic GC with [Fe/H] = −0.78 dex (Harris 1996; 2010 edition). M71 is an interesting cluster to study for a number of reasons. It has a metallicity similar to the well-studied southern GC 47 Tuc, which allows for comparisons to be drawn between the two. M71 also has a handful of previous measurements of the CN and CH bands (although with much smaller sample sizes), which means it is the perfect candidate for a high metallicity comparison for our method of determining multiple populations outlined in G18. Na and O measurements and *HST* UV photometry also exist for

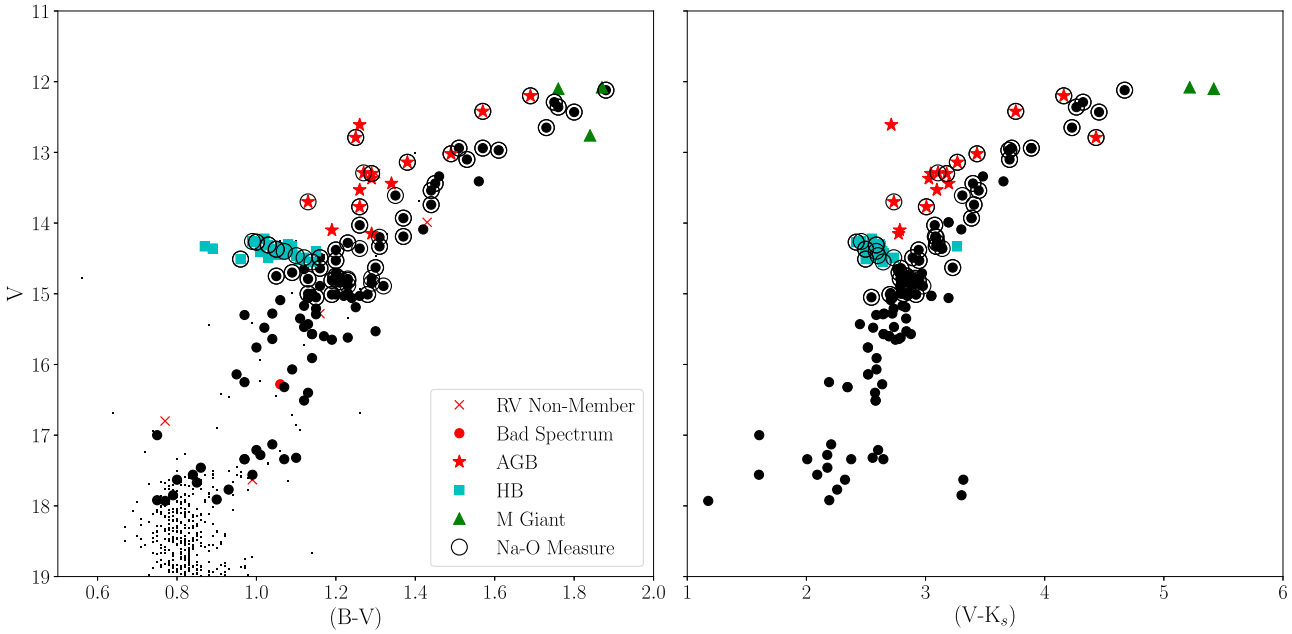

Figure 1. Left Panel: CMD for M71 using *B* and *V* photometry from Cudworth (1985 and private communication). Stars shown have an 85% or higher probability of being cluster members based on their proper motions Cudworth (1985 and private communication). Stars in our sample are indicated as large filled circles for RGB, red stars for AGB, and blue squares for HB. Three stars determined to be M giants are shown as green triangles. Stars with Na and/or O measurements are circled (Sneden et al. 1994; Ramírez & Cohen 2002; Carretta et al. 2009a, 2009b; Cordero et al. 2015). Right Panel: CMD for M71 using *V* photometry from Cudworth (1985 and private communication) and K_s photometry from 2MASS (Skrutskie et al. 2006). Symbols are the same as the left panel.

this cluster, which allows us to make comparisons across methods of identifying multiple populations.

By studying the CN and CH bands in the near-UV, low-resolution spectra for 101 RGB, 15 AGB, and 27 horizontal-branch stars (HB stars) in this cluster, we are able to classify stars into first and second generation across multiple evolutionary stages. We also focus on stars with Na–O measurements to compare classification methods and see if stars are classified into different populations based on what method is used. Recent studies (e.g., Smith et al. 2013; Smith 2015a, 2015b; Boberg et al. 2016) have revealed the presence of possible outliers classified differently depending on whether Na or CN is used. Our larger sample size allows us to see just how prevalent these outliers are and determine if they are a statistically significant group of stars.

2. Data

2.1. Observations and Target Selection

We obtained 171 combined spectra of stars within a 18′ by 18′ grid around the center of M71 between four observation runs in 2014 August, 2015 June, 2016 June, and 2017 June using the Wisconsin-Indiana-Yale-NOAO (WIYN)[1] 3.5 m Telescope and Hydra, a multi-object, fiber-fed bench spectrograph. The Bench Spectrograph was used with the "600@10.1" grating, which resulted in spectra with a ∼4.5 Å pixel^{-1} dispersion covering a range of ∼2800 Å. The spectra taken during the 2014 run are centered on a wavelength of 4900 Å, while the spectra taken in subsequent runs are centered on a wavelength of 5100 Å. Ten different configurations of fibers were necessary to obtain our full sample size.

We selected our target stars based on their location in the *V* versus (*B*–*V*) color–magnitude diagram (CMD) using photometry from Cudworth (1985 and private communication). The final selection included stars from the tip of the RGB down to the MSTO, which occurs at a $V \sim 18$ and is shown in Figure 1. We only observed stars with an 85% or greater likelihood of being cluster members based on proper motions determined by Cudworth (1985 and private communication). We also chose to observe as many stars as possible with Na and/or O measurements by Sneden et al. (1994), Ramírez & Cohen (2002), Carretta et al. (2009a, 2009b), or Cordero et al. (2015). Stars with measured Na and/or O abundances are indicated in Figure 1. Our final selection covers ∼2.5 half-light radii from the cluster center, and allows us to study trends of the properties of multiple populations with both magnitude and radial distance from the cluster's center.

2.2. Data Reduction and Radial Velocities (RV)

We reduced the data with the IRAF[2] package, dohydra to perform bias subtraction, flat-fielding, and dispersion correction with a CuAr comparison lamp spectrum. Final one-dimensional spectra were then produced using dohydra, as well. We exposed configurations of brighter cluster stars (with $M_v \leqslant 0.5$) for a total integration time of ∼1 hr over 7–10 exposures and configurations of faint stars (with $M_V > 0.5$) for a total integration time of ∼2.5–3 hr over 5–6 exposures to reduce the effects of cosmic rays and prevent saturation of the CCD. The processed spectra from each exposure were combined using the IRAF task scombine.

After reducing the spectra, radial velocities (RV) for each star were determined using the IRAF task fxcor by cross-

[1] The WIYN Observatory is a joint facility of the University of Wisconsin–Madison, Indiana University, the National Optical Astronomy Observatory, the University of Missouri, and Purdue University.

[2] IRAF is distributed by the National Optical Astronomy Observatory, which is operated by the Association of Universities for Research in Astronomy (AURA) under cooperative agreement with the National Science Foundation.

Table 1
Stars Measured in M71

ID[1]	R.A.[1] (J2000)	Decl.[1] (J2000)	RV_{hel} (km s^{-1})	V[1] (mag)	$(B-V)$[1] (mag)	M_V^2 (mag)	ID_{2MASS} (K)	T_{eff}	log g	S(3839)	CN(4216)	CH(4300)	δS(3839)	δCN(4216)	[Na/Fe]	[O/Fe]	Na Source[3]	O Source[3]	Branch[4]	Memb
2	298.406125	18.749889	−26	12.94	1.57	−0.85	19533747+1844596	4091	1.38	0.031	0.212	0.361	−0.123	−0.084	0.130	0.360	Cord	Cord	RGB	y
3	298.455875	18.740778	−23	12.08	1.87	−1.62	19534941+1844269	3601	0.41	…	…	…	…	…	…	…	…	…	M	y
5	298.464542	18.801667	−22	12.29	1.75	−1.44	19535150+1848059	3869	0.93	−0.157	0.202	0.347	−0.081	−0.081	0.320	0.520	Cord	Cord	RGB	y
6	298.444167	18.778083	−22	13.34	1.46	−0.39	19534660+1846411	4314	1.74	0.078	0.180	0.360	−0.201	−0.076	…	…	…	…	RGB	y
9	298.401125	18.824889	−25	13.41	1.56	−0.44	19533626+1849297	4257	1.67	0.335	0.327	0.346	0.076	0.071	…	…	…	…	RGB	y
14	298.362875	18.766361	30	13.30	1.30	−0.52	19532709+1845588	4727	1.94	0.380	0.265	0.367	0.162	0.130	…	…	…	…	AGB	n
15	298.371875	18.766222	−23	13.74	1.44	−0.08	19532925+1845584	4416	1.93	0.085	0.155	0.363	−0.212	−0.075	0.228	0.281	Car09a	Car09a	RGB	y
22	298.413250	18.734167	−24	13.93	1.37	0.17	19533918+1844030	4398	2.02	0.097	0.154	0.371	−0.198	−0.083	0.150	0.560	Cord	Cord	RGB	y
23	298.416125	18.731389	−22	12.94	1.51	−0.82	19533986+1843530	4173	1.46	0.305	0.372	0.353	0.091	0.122	0.340	0.050	Cord	Cord	RGB	y
27	298.510625	18.762056	−23	14.10	1.19	0.31	19540255+1845434	4976	2.40	−0.014	0.106	0.340	−0.077	−0.006	…	…	…	…	AGB	y
32	298.503083	18.818333	−19	12.61	1.26	−1.12	19540075+1849061	5007	1.84	0.366	0.332	0.309	0.325	0.250	…	…	…	…	AGB	y
37	298.406583	18.791250	−31	12.65	1.73	−1.17	19533757+1847286	3935	1.11	−0.076	0.214	0.345	−0.077	−0.098	0.509	0.396	Car09b	Car09b	RGB	y
38	298.409042	18.780472	26	13.99	1.43	0.23	19533817+1846497	4551	2.14	0.393	0.443	0.360	0.109	0.278	…	…	…	…	RGB	n
39	298.394625	18.772611	−21	14.09	1.42	0.27	19533470+1846213	4498	2.12	0.054	0.154	0.354	−0.240	−0.053	…	…	…	…	RGB	y
44	298.468125	18.748389	−29	14.03	1.26	0.30	19535236+1844542	4630	2.21	0.361	0.326	0.305	0.101	0.152	0.450	0.160	Cord	Cord	RGB	y
45	298.479417	18.759583	−22	13.77	1.26	−0.02	19535507+1845344	4742	2.15	0.118	0.131	0.350	−0.092	−0.011	0.390	0.530	Cord	Cord	AGB	y
46	298.471833	18.779750	−19	12.20	1.69	−1.56	19535325+1846471	3946	0.96	−0.057	0.250	0.350	−0.071	−0.054	0.180	0.330	Cord	Cord	AGB	y
47	298.474958	18.784250	−15	12.76	1.84	−1.00	19535399+1847034	3485	0.19	…	…	…	…	…	…	…	…	…	M	y
48	298.483708	18.787972	16	12.10	1.76	−1.63	19535610+1847167	3568	0.30	…	…	…	…	…	…	…	…	…	M	y
49	298.490167	18.799167	−26	13.44	1.45	−0.29	19535764+1847570	4374	1.82	0.343	0.366	0.317	0.051	0.133	0.660	0.230	Cord	Cord	RGB	y
52	298.461000	18.818722	−25	12.97	1.61	−0.76	19535064+1849075	4175	1.49	0.244	0.384	0.322	0.029	0.139	0.820	0.220	Cord	Cord	RGB	y
53	298.463333	18.808583	−23	14.36	1.26	0.63	19535120+1848308	4666	2.37	−0.007	0.121	0.336	−0.253	−0.037	0.200	…	Cord	…	RGB	y
55	298.451167	18.807028	−18	13.14	1.38	−0.59	19534828+1848253	4473	1.76	0.398	0.370	0.323	0.102	0.211	0.420	0.350	Cord	Cord	AGB	y
61	298.451125	18.800611	−21	12.36	1.76	−1.34	19534827+1848021	3882	0.98	0.021	0.309	0.380	0.081	0.023	0.680	0.110	Cord	Cord	RGB	y
62	298.446458	18.800333	−20	13.44	1.34	−0.26	19534715+1848012	4513	1.92	0.150	0.159	0.373	−0.142	−0.047	…	…	…	…	AGB	y
63	298.440625	18.798583	−14	12.43	1.80	−1.27	19534575+1847547	3810	0.92	−0.141	0.217	0.352	0.008	−0.059	0.230	0.310	Cord	Cord	RGB	y
64	298.444000	18.795583	−26	13.53	1.26	−0.17	19534656+1847441	4593	2.00	0.403	0.297	0.345	0.130	0.123	…	…	…	…	AGB	y
65	298.442292	18.790556	−19	13.10	1.53	−0.60	19534615+1847261	4159	1.54	0.020	0.202	0.355	−0.185	−0.093	0.360	0.440	Cord	Cord	RGB	y
66	298.432208	18.792667	−28	13.54	1.44	−0.25	19534373+1847336	4370	1.83	0.082	0.164	0.345	−0.210	−0.067	0.436	0.384	Car09a	Car09a	RGB	y
68	298.428667	18.777056	−26	13.70	1.13	−0.06	19534288+1846374	5007	2.26	0.008	0.108	0.325	−0.033	−0.005	0.330	…	Cord	…	AGB	y
71	298.420958	18.768222	−25	13.30	1.29	−0.37	19534103+1846056	4584	1.92	0.442	0.342	0.325	0.166	0.163	0.400	0.310	Cord	Cord	AGB	y
72	298.428375	18.770278	−25	14.15	1.29	0.42	19534282+1846129	4616	2.25	0.064	0.126	0.355	−0.201	−0.059	…	…	…	…	AGB	y
75	298.432125	18.770944	−28	14.33	0.87	0.60	19534371+1846154	5597	2.77	0.111	0.140	0.233	0.403	0.081	…	…	…	…	HB	y
77	298.436708	18.763500	−22	14.26	0.99	0.53	19534480+1845486	5304	2.63	0.136	0.155	0.269	0.291	0.094	0.520	…	Cord	…	HB	y
78	298.440083	18.763944	−21	14.37	1.05	0.64	19534561+1845502	5258	2.66	−0.032	0.076	0.330	0.096	0.004	0.230	0.560	Ram	Ram	HB	y

Note. 1. Cudworth (1985 and private communication), 2. Assuming $(m-M)_v = 13.728$, 3. Sneden et al. (1994), Ramírez & Cohen (2002), Carretta et al. (2009a, 2009b), or Cordero et al. (2015), 4. M indicates a star with spectral type M The complete table is available online.

(This table is available in its entirety in machine-readable form.)

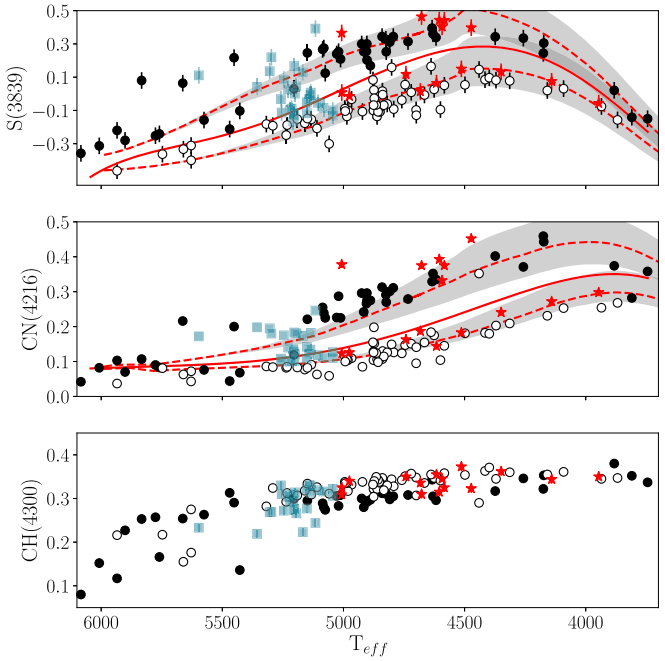

Figure 2. S(3839), CN(4216), and CH indices plotted against effective temperature, top, middle, and bottom panel, respectively. Points are indicated as in Figure 1, with the exception that CN-enhanced RGB stars are indicated as filled circles and CN-normal RGB stars are indicated as open circles. Error bars showing the estimated uncertainty are shown in each panel. For CN(4216) and CH, the estimated uncertainty is smaller than the points. Solid red lines in the top two panels are the fiducial lines used to create a δS(3839) and a δCN(4216) index. Dashed red lines indicate fiducials with a given C and N abundance: [C/Fe] = −0.3 dex, [N/Fe] = 1.5 dex for the CN-enhanced, and [C/Fe] = 0.0, [N/Fe] = 0.6 dex for the CN-normal. The shaded, gray areas around these fiducials represent the uncertainty from the range in [O/Fe] abundances for these stars as discussed in Section 3.3.

correlating with an RV standard star, HD 107328, observed during the 2016 and 2017 runs. For the 2014 and 2015 runs, RV measurements were made using the 2017 observations of the standard star. To check for consistency between standards used, we also made RV measurements using the 2016 observations of the same standard star, and no systematic differences were found. All four runs showed further agreement by having similar medians, and stars with multiple observations across different runs were also found to have RV measurements that agreed within uncertainties and showed no systematic offsets between runs. The final RV measurements for each star are given in Table 1 along with positions and photometry from Cudworth (1985 and private communication). Uncertainties on RV measurements made with this method at this resolution are around 15 km s^{-1}. We determined a median RV of −23 km s^{-1} with a standard deviation of 6.5 km s^{-1} for the cluster, which agrees well with what was found by high resolution studies of Peterson & Latham (1986) (-22.1 ± 0.8 km s^{-1}), Cohen et al. (2001) (-21.7 ± 2.6 (s.t.d.) km s^{-1}), and Kimmig et al. (2015) (-23.1 ± 0.3 km s^{-1}).

Final membership was determined using a similar method as in G18; stars with radial velocities falling outside of three standard deviations from the cluster median when calculated using the entire sample were deemed as non-members. Because our stars were selected based on a proper motion study, we do not have many non-members in our sample. Our sample includes 171 RV measurements, with 5 stars being RV non-members shown in Figure 1 as red crosses. Of the remaining spectra, 20 were multiple measurements of stars across nights or observing runs to use to determine uncertainties and one was found to have a bad spectrum (too low signal-to-noise ratio (S/N)). This leaves the final number of likely member stars observed as 145, with 100 RGB, 15 AGB, 27 HB stars, and 3 stars determined to be M giants also shown in Figure 1. 2MASS photometry was used to identify AGB and HB stars as the relatively high amount of extinction toward the direction of M71 made stars difficult to classify in the optical CMD; the RGB, AGB, and HB sequences were much more clearly defined in the IR photometry, as shown in the right panel of Figure 1.

3. Analysis—CN and CH Bands

3.1. Index Definitions

Following our previous work (G18), we used the CN index at ∼3885 Å, S(3839), and the commonly used CH index at ∼4300 Å as defined by Harbeck et al. (2003). We were also able to use the CN index at ∼4140 Å, CN(4216), due to the relatively high metallicity of M71 stars (Friel 1987). The higher metallicity allows the redder CN band, which is the weaker and broader of the two bands, to be strong enough to give significant measurements and show a difference between the two populations. We used the CN(4216) index as defined by Friel (1987) rather than the commonly used S(4142) index from Norris & Freeman (1979) because CN(4216) is a double-sided index and therefore less likely to be affected by any problems with the continuum levels of the spectra. Our final index definitions are as follows:

$$\mathrm{S}(3839) = -2.5 \log \frac{F_{3861-3884}}{F_{3894-3910}} \quad (1)$$

$$\mathrm{CN}(4216) = -2.5 \log \frac{F_{4144-4177.75}}{0.5F_{4082-4118.25} + 0.5F_{4246-4284.75}} \quad (2)$$

$$\mathrm{CH}(4300) = -2.5 \times \log \frac{F_{4285-4315}/30}{0.5(F_{4240-4280}/40) + 0.5(F_{4390-4460}/70)}. \quad (3)$$

3.2. Flux Calibration

We followed the method used in G18 to flux calibrate the spectra using model spectra generated by the Synthetic Spectrum Generator (SSG; Bell et al. 1994, and references therein) using MARCS model atmospheres (Gustafsson et al. 2008). We used a metallicity of [Fe/H] = −0.78 (Harris 1996 (2010 edition)). As in G18, effective temperatures for the model spectra were calculated from the V–K colors of the stars based on the method by Alonso et al. (1999, 2001) with V magnitudes from Cudworth (1985 and private communication) and K magnitudes from 2MASS (Skrutskie et al. 2006). K magnitudes were corrected to the TCS system following the method by Johnson et al. (2005). If a star did not have a K magnitude, the relation for effective temperature based on B–V color was used (Alonso et al. 1999).

M71 is located at a low Galactic latitude and therefore suffers from more extinction than most other GCs. Measurements for the reddening of the cluster range from $E(B–V)$ = 0.21 to 0.32 (Brasseur et al. 2010, and references therein). We note that differences also seem to exist depending on what photometric filters were used to derive the $E(B–V)$ for the

cluster. For example, studies matching models to CMDs using filters in the optical region tend to find a higher $E(B-V)$ of 0.28 (Grundahl et al. 2002; Morrison et al. 2016), while studies matching CMDs in the infrared tend to find a lower $E(B-V)$ of 0.22 (Brasseur et al. 2010). Because of these discrepancies and the fact that we had to use a mixture of infrared and optical colors to determine accurate temperatures, we selected an $E(B-V)$ between these values that allowed for the highest consistency between effective temperatures calculated with $B-V$ and $V-K$ colors. This method ensured that all of our stars were on the same temperature scale whether they had accurate IR photometry or not. Recent photometric studies of M71 have also indicated that there is differential extinction across the cluster (Morrison et al. 2016), so we used the reddening map from Morrison et al. (2016) to correct for differential extinction, which can cause changes in the $E(B-V)$ value up to 0.08.

Surface gravities were calculated using the bolometric corrections given by Alonso et al. (1999) and are listed with the effective temperature for each star in Table 1. Absolute magnitudes were calculated for each star using an apparent distance modulus of $(m-M)_V = 13.728$ from Morrison et al. (2016) and an extinction value for each star calculated using the reddening from Morrison et al. (2016). These are also given in Table 1.

3.3. Band Measurements

We measured CN and CH band strengths of the flux calibrated spectra and plotted the measurements versus effective temperature as shown in Figure 2. Uncertainties on our band strength measurements were calculated as in G18. The standard deviation of band strengths for stars that were measured across multiple nights or runs was determined for faint ($M_V \geqslant 1.0$) and bright ($M_V < 1.0$) stars. The uncertainty was roughly the same for both magnitude groups, so a combined median standard deviation was taken for all stars as representative of the uncertainty in our measurements. This method gives uncertainties of 0.1 for the S(3939) index, 0.05 for the CN(4216) index, and 0.05 for the CH(4300) index.

In G18, we showed how the CN and CH band strengths are affected by effective temperature and surface gravity by plotting them versus absolute magnitude (luminosity). For this paper, we have chosen to plot band strengths versus effective temperature instead, so that stars in different evolutionary stages (RGB, AGB, and HB) all follow similar trends. By plotting versus effective temperature, we help offset effects other than abundances that cause changes in band strengths between different evolutionary stages at a given magnitude, such as AGB and HB stars being hotter than RGB stars.

Looking at the S(3839) band in the top panel of Figure 2, there is a clear spread in CN band strength that would indicate the presence of multiple populations, but populations do not separate themselves very clearly as in M10 (G18). However, the middle panel of Figure 2 shows two populations clearly separated in CN(4216) strength similar to what was seen by Briley et al. (2001b) in DDO photometry of RGB stars in M71. While this separation seems certain enough to classify stars in M71 by eye alone, we still needed to create an objective classification method for two reasons. The first is that the CN(4216) band becomes too weak at the higher effective temperatures of the faintest stars to be sensitive to abundance differences and therefore cannot be used to classify the faintest stars in our sample ($M_V \geqslant 3.0$; $T_{\rm eff} \geqslant 5300$ K). Second, since the CN(4216) band cannot be used to classify the faintest stars, we must rely on the S(3839) band, but because the populations do not separate as clearly in the S(3839) band, an objective classification method is required.

To classify populations objectively, we followed the same method as that in G18 by modeling the atmospheric effects on the band strengths and creating a δCN index. Atmospheric effects were modeled by generating synthetic spectra with the SSG. Effective temperatures and surface gravities were taken from a 12 Gyr PARSEC isochrone (Marigo et al. 2017). An age of 12 Gyr was chosen based on the age for the cluster found by Di Cecco et al. (2015).

We based carbon and nitrogen abundances for these spectra on the studies of Briley & Cohen (2001a) and Briley et al. (2001b, 2004). Briley et al. (2001b) found two populations of RGB stars in DDO photometry of the CN(4216) band and were able to match sets of carbon and nitrogen abundances to each population. The CN-normal population approximately matched a [C/Fe] of 0.0 dex and a [N/Fe] of 0.4 dex, while the CN-enhanced population approximately matched a [C/Fe] of −0.3 dex and a [N/Fe] of 1.4 dex. The same sets of abundances were then found to match S(3839) and CH band measurements of main-sequence stars by Briley & Cohen (2001a). These bands were then used to make abundance measurements for individual stars by Briley et al. (2004), which also agreed with those previously measured for each population.

We used these carbon and nitrogen abundances as starting points to find a carbon and nitrogen abundance that would match each population in the S(3839) and CN(4216) band strengths. Since the work by Briley & Cohen (2001a) and Briley et al. (2001b, 2004), oxygen abundances have been measured for large samples of stars in M71 (Carretta et al. 2009a, 2009b; Cordero et al. 2015), so some adjustments had to be made to these abundances. The measured oxygen abundances were slightly higher than those assumed by Briley & Cohen (2001a) and Briley et al. (2001b, 2004), which means that the nitrogen abundances had to be raised to match CN band strengths. We find that a fiducial created with [C/Fe] = −0.3 dex and [N/Fe] = 1.5 dex approximately matches the CN-enhanced population, and a fiducial with [C/Fe] = 0.0 dex and [N/Fe] = 0.6 dex matches the CN-normal population. We used an [O/Fe] = 0.3 dex and [O/Fe] = 0.41 dex for the CN-enhanced and CN-normal populations, respectively, based on the measurements from various sources (Sneden et al. 1994; Ramírez & Cohen 2002; Carretta et al. 2009a, 2009b; Cordero et al. 2015). We also had to take into account that the surface $^{12}C/^{13}C$ changes in GC RGB stars as they climb the giant branch due to secondary mixing. We followed the same method as Simpson et al. (2017) and Kirby et al. (2015), who also studied RGB stars in GCs and adjusted the $^{12}C/^{13}C$ as a function of surface gravity based on measurements shown in Figure 4 in Keller et al. (2001).

When creating fiducial lines in the S(3839) versus M_V for M10 in G18, we had to take the change in abundance as a function of magnitude into account. We determined this was not necessary for M71, as the efficiency of extra mixing will be lower for a higher metallicity cluster. Smith et al. (2007) showed that the variation of [C/Fe] as a function of magnitude for some of the brightest stars in M71 is less than 0.2 dex. The final fiducial lines for each population are plotted in Figure 2 as red dashed lines with each line matching the corresponding population relatively well in both CN band strengths. These

fiducial lines also have a certain amount of uncertainty caused by the spreads in oxygen found in each population (Sneden et al. 1994; Ramírez & Cohen 2002; Carretta et al. 2009a, 2009b; Cordero et al. 2015). The [O/Fe] for the CN-normal population ranges from 0.1 to 0.6 dex, and 0.0 to 0.6 dex for the CN-enhanced population. The shaded areas around each population fiducial shown in Figure 2 represent the uncertainties caused by spreads between these values.

For the fiducial used to separate the two populations, we took the average carbon, nitrogen, and oxygen abundances from these CN-enhanced and CN-normal fiducials (i.e., [C/Fe] = −0.15, [N/Fe] = 1.0, [O/Fe] = 0.355 dex). Synthetic spectra were then used to create a fiducial average band strength for the S(3839) band and the CN(4216) band, which are plotted in Figure 2 as solid red lines. A δS(3839) index and a δCN(4216) index were generated by subtracting the S(3839) and CN(4216) band strengths from their given average fiducials (see G18 for more details).

RGB stars with a positive δS(3839) index are considered CN-enhanced stars and are represented in Figure 2 as closed circles, while stars with a negative δS(3839) index are CN-normal and shown as open circles. We keep this designation for all three panels in Figure 2. In the middle panel of Figure 2, the two populations classified by the S(3839) index fall exactly where one would expect for the stars cool enough ($T_{\rm eff} \leqslant$ 5300 K) to have CN(4216) band strengths sensitive to changes in abundance except for two stars. One of these stars is enhanced in δS(3839), but not in δCN(4216). This difference can be explained by the fact that it is one of the brightest stars in the sample, and the S(3839) band is not very sensitive to differences in abundances at that magnitude. The other star is one that is enhanced in CN(4216) and not in S(3839), which is due to the spectrum for this star having lower S/N than the others. Since our sensitivity decreases toward bluer wavelengths, the bluer S(3839) band was more heavily affected by low S/N and resulted in too low a measurement. While the CN(4216) index was not used directly for classification, it provides confidence in our classification method because both bands seem to give consistent assignment to populations of stars in the cluster.

4. Results and Discussion

4.1. Multiple CN Populations in M71

4.1.1. RGB Stars

Following G18 and as discussed in Section 3.3, we used the δS(3839) index to sort the RGB stars in M71 into CN-enhanced and CN-normal populations. The measured δCN(4216) versus δS(3839) index for the RGB stars in our sample is shown in Figure 3. In general, the two δCN bands correlate well with one another as expected from Figure 2. There is a small group of stars with high δS(3839) and low δCN(4216), which are the fainter stars in the sample. For these stars, the surface temperature becomes hot enough that the CN(4216) band is no longer sensitive to changes in abundance ($T_{\rm eff} \geqslant$ 5300 K).

The presence of at least two populations is evident from the histograms of δS(3839) and δCN(4216) along the x- and y-axes of Figure 3. However, in order to test whether M71 hosts additional populations, as detected in a few Galactic clusters (see, e.g., Carretta et al. 2009a, 2009b; Carretta 2015; Milone et al. 2015a, 2015b), we have calculated the number of populations by applying a Gaussian mixture model (GMM) to

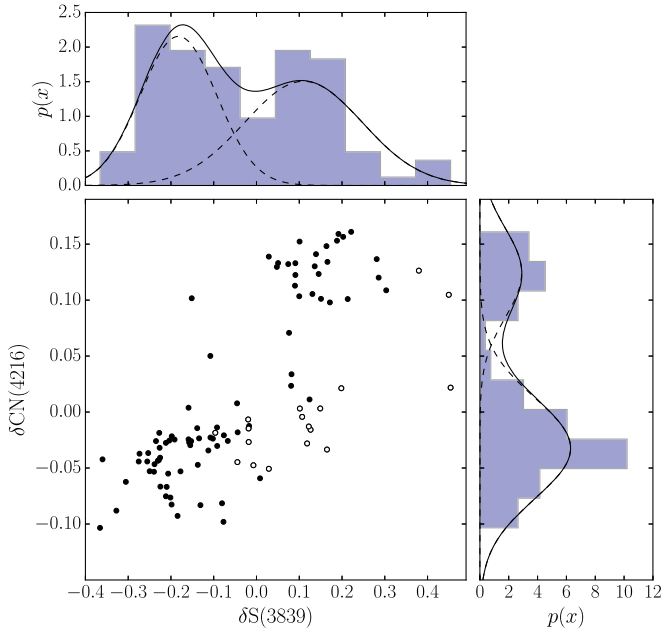

Figure 3. δCN(4216) versus δS(3839) for the RGB stars in our sample. RGB stars with $T_{\rm eff} > 5300$ K are indicated as open circles. Histograms for each axis are shown with fits based on Gaussian Mixture Models overplotted.

the δS(3839) and δCN(4216) distributions. The Bayesian and Akaike information criteria (BIC and AIC, respectively) are used to quantify the success of fitting different models with different numbers of populations. The model with the number of populations that minimizes both criteria is accepted as the best fit. For both the δS(3839) and the δCN(4216) distributions, the BIC and AIC were minimized with two Gaussians (one for each population). The CN-enhanced population had an average δS(3839) of 0.18 and an average δCN(4216) of 0.125, while the CN-normal population had an average δS(3839) of −0.17 and an average δCN(4216) of −0.025. The final GMM fits to each distribution are plotted in Figure 3.

Based on this information and our δS(3839) index, we find that 42 out of 100 or 42% ± 4% of RGB stars are CN-enhanced and belong to the second generation, making M71 a first generation dominated cluster. Our uncertainty comes from propagating uncertainties based on counting statistics, through the calculation of the ratio of second generation stars to the total stars in our sample. This ratio agrees with what is found using photometry centered on the S(3839) band by Bowman et al. (2017), who found roughly 45% of stars belonging to the second generation. However, the result disagrees with that found in the Na–O distribution by Carretta et al. (2009b) and Cordero et al. (2015), with the latter finding M71 to be dominated by Na-enhanced stars, with 71% belonging to the second generation (using [Na/Fe] = 0.2 dex as a separating value). We leave our discussion on the possible reason for this disagreement to a later section (Section 4.3.1), where we compare to other methods of identifying multiple populations.

4.1.2. AGB Stars

Recently, there has been some debate as to whether or not all populations found in GCs exist at all stages of stellar evolution after the RGB; specifically, an absence of the second generation on the AGB has been reported in clusters such as

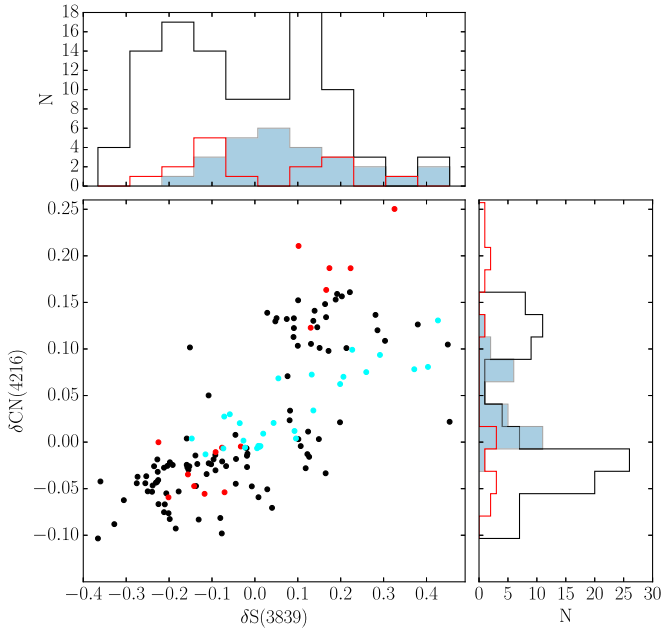

Figure 4. δCN(4216) versus δS(3839) for all stars in our sample. RGB stars are shown as black, AGB as red, and HB as blue points. Histograms for each axis are shown with color coding that matches the color coding for the points.

NGC 6257 (Campbell et al. 2012, 2013) and M4 (MacLean et al. 2016), while second generation AGB stars have been observed in other clusters—namely, 47 Tuc, M13, M5, M3, M2, and NGC 6397 (García-Hernández et al. 2015; Johnson et al. 2015; MacLean et al. 2018; see also Section 4.1.1 of G18 for further discussion and details on multiple populations in AGB stars).

In Figure 4, we add the distributions of δS(3839) and δCN (4216) for the AGB and HB stars in M71 to Figure 3 as red and blue points, respectively. From Figure 4 it seems that the AGB stars roughly follow the distribution of the RGB stars, with the only difference being a couple of stars with slightly higher δCN (4216) values. The AGB stars also separate very clearly into two populations in both the δS(3839) and δCN(4216) bands. However, as stated in G18, classifying AGB stars by comparing a δCN measurement to RGB stars without other considerations can lead to misclassification. This misclassification stems from the fact that while δCN can be used as a proxy for the underlying N abundance, the band is also dependent on other abundances that should be considered—particularly the C abundance. To further ensure that the distribution of the CN band was due to similar differences in underlying N abundances between RGB and AGB stars, we also compared the distribution of the CH band strengths to the RGB stars since it is independent of the N abundance.

The right panel of Figure 5 shows the CH band measurements for just the AGB and RGB stars in M71. The CH bands for the AGB stars match well with the CH bands for the RGB stars with similar $T_{\rm eff}$, which is expected due to the less efficient extra mixing in a cluster of this metallicity. For comparison, we also show the CH band measurements from G18 from the RGB and AGB stars in M10 in the left panel of Figure 5. The AGB stars in this cluster have lower CH band measurements compared to RGB stars with similar $T_{\rm eff}$ because the extra mixing is more efficient at the lower metallicity of M10 and causes stars to have lower surface carbon abundances than RGB stars by the time they reach the

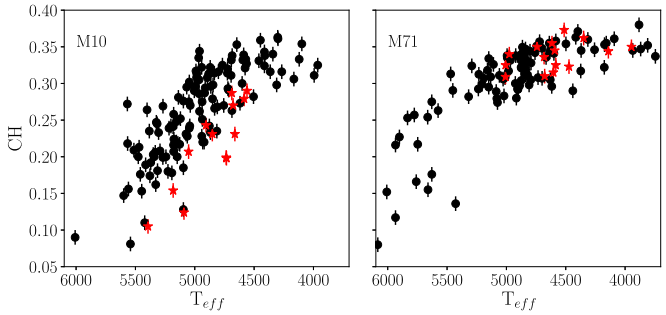

Figure 5. CH(4300) band strength against effective temperature. Our measurements for M10 from G18 are shown on the left panel, and the results from this work for M71 are on the right. RGB stars are shown as black points and AGB stars are shown as red stars.

AGB phase. Thus the CH band can be used as an indication of whether or not the CN band can be used to securely sort AGB stars into populations. In the case of M71, we determine that since the CH bands of the AGB stars match the RGB stars, the separation in δCN index values between the two populations appearing in the AGB star distribution is caused by differences in N and not differences in C.

When using the same classification scheme as used for the RGB stars based on δS(3839), we find 6 CN-enhanced and 9 CN-normal AGB stars. If AGB stars are classified with the δCN(4216) index, the same distribution is found. This result equates to 40% ± 13% of AGB stars sampled being CN-enhanced, which agrees well with the distribution found in the RGB stars of 42% ± 4%. For M71, as in M10, it appears that there is no lack of the second generation stars on the AGB (G18).

4.1.3. HB Stars

Because the HB of M71 is relatively cool and red, we were able to obtain CN and CH measurements for 27 HB stars. We calculated δS(3839) and δCN(4216) indices for all HB stars using the same method as described in Section 3.3 for the RGB stars. Our final values for each δCN index for the HB stars are plotted in Figure 4 as blue points. From Figure 4, it appears that the HB stars separate into two populations similar to the RGB stars based on δCN(4216) band strength, where two peaks can be seen in the distribution shown on the *y*-axis. However, while there is a spread in the δS(3839) index among HB stars, the distribution does not easily separate into two groups. To make sure that there are indeed two populations in the HB stars, we turned to the CH band measurements to see what information could be added.

In Figure 6, we plot δS(3839) versus δCH for all of the stars in our sample. The δCH index was created by fitting the CH band strength versus $T_{\rm eff}$ plotted in the bottom panel of Figure 2 with a polynomial and subtracting this trend out of the CH band measurements. This method created a δCH measurement that was independent of temperature and surface gravity effects, and only depended on carbon abundance (similar to the δCN indices). Plotting the δS(3839) versus δCH shows an anti-correlation between these two measurements as expected for RGB, AGB, and HB stars. The HB stars also separate in this plot into two populations, one CN-enhanced and CH-weak, and one CN-normal and CH-normal. This result indicates that although the distribution in δS(3839) alone does not show the same clear separation in populations as the δCN(4216) index,

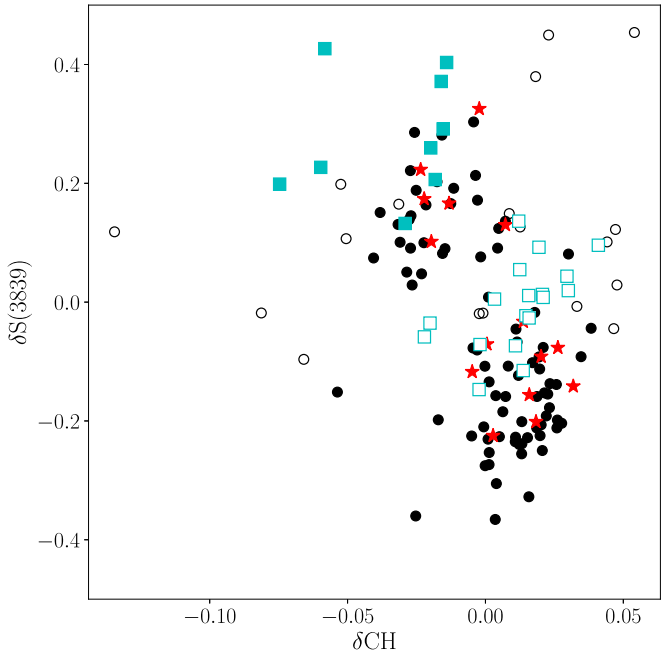

Figure 6. δS(3839) versus δCH for all stars in our sample. RGB, AGB, and HB stars are indicated as in Figure 1. RGB stars with $T_{\rm eff}>$ 5300 K are shown as open circles. HB CN-enhanced stars are cyan squares and CN-normal stars are open squares.

there are still two populations present in the HB stars, given the evidence of two separated groups in the δS(3839) versus δCH plot.

Because the HB stars separate into two groups more clearly in the δS(3839) versus δCH plot (Figure 6), we used this diagram to classify the HB stars in our sample. We classified HB stars with δS(3839) values above the line $\delta S(3839) = 4\delta CH + 0.2$ as CN-enhanced and those below the line were classified as CN-normal. These stars are coded in Figure 6 as open or closed squares for CN-normal and CN-enhanced, respectively. We find 9 CN-enhanced and 18 CN-normal stars on the HB, which gives 33% ± 9% of stars as CN-enhanced. This value agrees with the RGB stars within our uncertainties, and provides evidence that there is not a lack of CN-enhanced stars on the HB in M71.

A study of the metal-rich GC, 47 Tuc, found that the CN-enhanced and CN-normal populations had different HB morphologies in the CMD (Briley 1997). Since 47 Tuc has a metallicity similar to M71, with [Fe/H] = −0.72 (Harris 1996 (2010 edition)), we analyzed the location of the two populations in M71 on the HB to see if the same difference in morphology was observed. The left panel of Figure 7 shows a zoomed in look of the CMD from Figure 1 centered on the HB with CN-enhanced stars shown as closed squares and CN-normal stars shown as open squares. We also show as red triangles the average Mv and $(B–V)_0$ of each population, with their associated mean errors. Although the scatter among individual stars is large, the CN-enhanced HB stars are displaced systematically to brighter magnitudes and bluer colors than the CN-normal HB stars, by differences that are large compared to the mean error of the average values (see Table 2). This result is similar to what Briley (1997) found in 47 Tuc, where the locus of the CN-enhanced population was found to be 0.05 magnitudes brighter than the CN-normal population; for M71, we find a difference of 0.08 mag.

As Briley (1997) noted, a slight difference in He abundance between the two populations would cause a different zero-age horizontal-branch (ZAHB) location for each population. Multiple studies have now shown that the multiple populations observed in GCs have different He abundances (see, e.g., Milone et al. 2015a, 2018; Lagioia et al. 2018, etc.). Higher envelope He content in second generation stars would cause these stars to sit at slightly bluer colors and slightly higher luminosities on the HB, just as observed in M71. To quantify the difference in He abundance between the two populations, we generated two ZAHBs with differing He abundances running through the average HB position of each populations. These ZAHBs were generated with the PGPUC isochrones, using the online interpolater that can be found at http://www2.astro.puc.cl/pgpuc/index.php (Valcarce et al. 2012, 2013), and are shown in Figure 7. The right panel of Figure 7 shows the full CMD and isochrones generated with the PGPUC isochrone interpolator using the same parameters for the ZAHBs.

We found that the average position of the CN-enhanced stars is best fit by a ZAHB with $Y = 0.325$ and that of the CN-normal stars is best fit by a ZAHB with $Y = 0.30$. This difference of ΔY of 0.025 between the two populations agrees with the maximum ΔY found by Milone et al. (2018) using *HST* UV photometry, and confirms that the difference in average position on the HB between the two populations is likely caused by a difference in He abundance.

4.2. Distribution across the Cluster

Thanks to the large number of stars observed and the broad radial coverage extending to ∼2.5 half-light radii ($R_h = 1\farcm67$; Harris 1996, 2010 edition), we are able to analyze the radial distribution of the two populations found in M71. The bottom panel of Figure 8 shows the ratio of the number of CN-enhanced to the total number of RGB stars in radial bins with a width of ∼0.35 half-light radii. The top panel of Figure 8 shows a histogram of the distribution of stars used to calculate these ratios. The distribution from our sample using the δS (3839) index is shown as a black line in the top panel and as closed circles in the bottom panel. The distribution from a collection of Na abundance measurements from Sneden et al. (1994), Ramírez & Cohen (2002), Carretta et al. (2009a, 2009b), and Cordero et al. (2015) is shown as a red line in the top panel and as red squares in the bottom panel. The offsets we used to combine these samples come from Smith (2015b) and are discussed further in Section 4.3.1.

Based on the results shown in Figure 8, we found no significant change in the number ratio of CN-enhanced to CN-normal stars as a function of the radial distance from the cluster's center. We also compare this result to what is found if the stars are divided into first and second generation based on Na abundance. We decided to follow Carretta et al. (2009a, 2009b) and use [Na/Fe] = 0.3 dex to separate stars based on Na abundance instead of [Na/Fe] = 0.2 dex, which was used by Cordero et al. (2015). Figure 8 shows that while the ratio for Na-enhanced to Na-normal is different from that found in our study (see Section 4.1), when populations are identified using Na there is no significant radial variation in the ratio of Na-enhanced to Na-normal. Cordero et al. (2015) and Bowman et al. (2017) have studied the radial distribution of the two populations in M71 using Na abundance and narrow-band

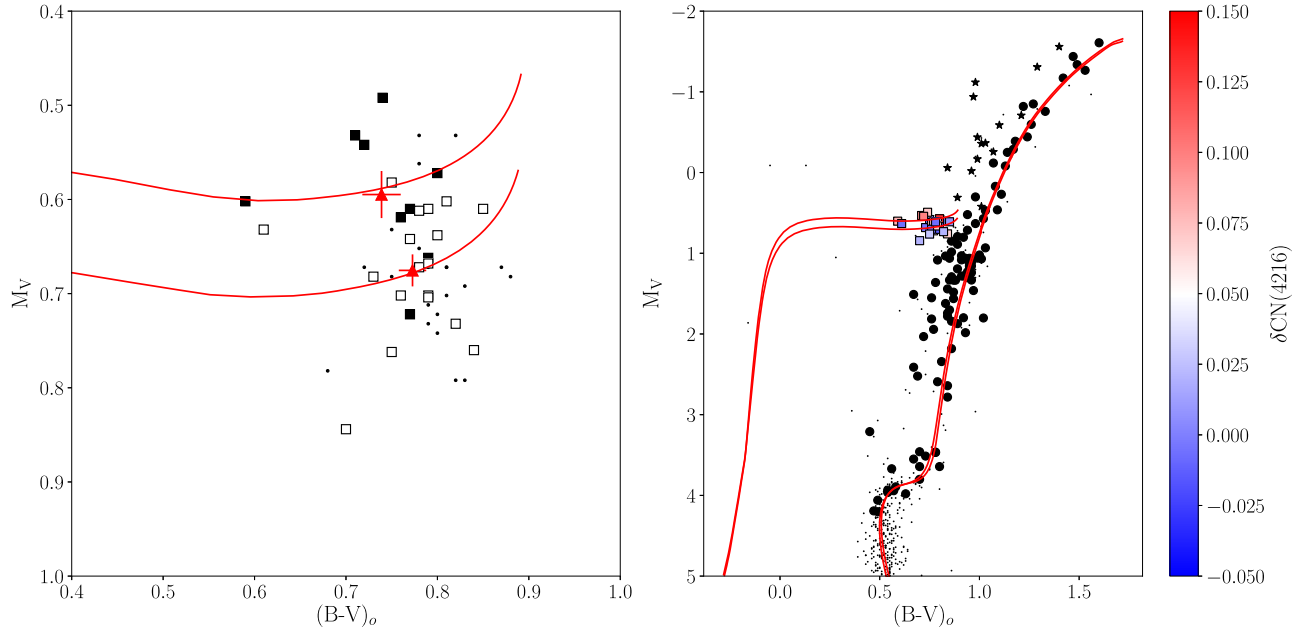

Figure 7. Left Panel: CMD for M71 centered on the HB with M_V versus $(B–V)_o$ (photometry from Cudworth 1985 and private communication). Small dots indicate HB stars (determined based on their position in the CMD) that have an 85% probability of membership determined by Cudworth (1985 and private communication) that were not measured for CN strength. HB stars are indicated as squares with open squares being CN-normal and filled being CN-enhanced following the same classification as shown in Figure 6. Average positions of each population are shown as red triangles with error bars indicating the mean errors. Red lines show the two ZAHBs that best fit these positions. Right Panel CMD of M71 with HB stars indicated as colored squares color-coded based on their δCN(4216) band strength, as indicated by the color bar to the right. Black circles are RGB stars, and stars are AGB stars. Overplotted are red lines showing the ZAHBs from the left panel, as well as isochrones generated with the same parameters using the PGPUC isochrone interpolator.

Table 2
Mean HB Positions

Population	M_V	$(B–V)_o$
CN-enhanced	0.595 ± 0.07 (σ)	0.739 ± 0.06 (σ)
	± 0.025 (m.e.)	± 0.021 (m.e.)
CN-normal	0.675 ± 0.07 (σ)	0.773 ± 0.06 (σ)
	± 0.017 (m.e.)	± 0.015 (m.e.)
Δ	0.08	0.034

photometry centered on the S(3839) band, respectively, and both studies agree with our result that there is no radial change in the number ratio of the two populations.

While all formation scenarios for multiple populations agree that second generation stars are originally more centrally concentrated (see, e.g., Decressin et al. 2007a, 2007b; D'Ercole et al. 2008; Bekki 2010), the results of Figure 8 are not surprising considering that M71 is a dynamically old cluster. As Cordero et al. (2015) and Bowman et al. (2017) have pointed out, $t/t_{\rm rh} \sim 44$ for M71 considering a cluster age of 12 Gyr (Di Cecco et al. 2015) with $t_{\rm rh}$ being the half-mass relaxation time. For comparison, 47 Tuc, a cluster with a similar age and metallicity, has a much younger dynamical age of $t/t_{\rm rh} \sim 3$ (using $t_{\rm rh}$ value from Harris 1996, 2010 edition) and is observed to have a more centrally concentrated second generation compared to the first generation (Milone et al. 2012; Cordero et al. 2015). Other examples of clusters with more concentrated second generation stars can be found in Bellini et al. (2009), Lardo et al. (2011), Carretta et al. (2010), Johnson & Pilachowski (2012), Milone et al. (2012), and Simioni et al. (2016). Clusters in which second generation stars are still more concentrated than first generation stars tend to be, in general, dynamically younger (see, e.g., Dalessandro et al. 2019, for a recent observational study of the dependence of the degree of spatial mixing on clusters' dynamical age).

However, the simulations from Vesperini et al. 2013 have shown that as clusters experience the effects of internal relaxation and mass loss, these radial gradients in the populations' number ratio are gradually erased, and dynamically old clusters may reach complete spatial mixing. In particular, Vesperini et al. (2013) found that to reach complete spatial mixing as observed in M71, M10 (G18), and a variety of other clusters (see also Dalessandro et al. 2014; Nardiello et al. 2015), a cluster must have lost 60%–70% of its initial mass due to two-body relaxation (see also Miholics et al. 2015). Evidence for M71 having experienced enough mass loss to reach complete spatial mixing comes from multiple sources such as the flattened stellar mass function (De Marchi et al. 2007). Carretta et al. (2010) have suggested that the excess X-ray sources found in the cluster by Elsner et al. (2008) also imply that the cluster has experienced significant mass loss. Finally, a cluster's mass-loss rate is enhanced by the stronger tidal field of the inner regions of the Galaxy (see e.g Vesperini & Heggie 1997; Baumgardt & Makino 2003). Dinescu et al. (1999) determined the orbit of M71 is confined within 6.7 kpc, and according to the recent orbital parameters' determination based on *Gaia* data (Helmi et al. 2018), the pericenter of M71's orbit is at about 5 kpc from the Galactic center and its apocenter at about 7.2 kpc. These results suggest that the cluster is indeed likely to have experienced significant mass loss.

4.3. Comparison to Other Definitions of Multiple Populations

4.3.1. Na–O Anti-correlation

Multiple populations in GCs have differences in their Na and O abundances as well as their C and N abundances. Due to the various nucleosynthesis processes in the progenitors of the

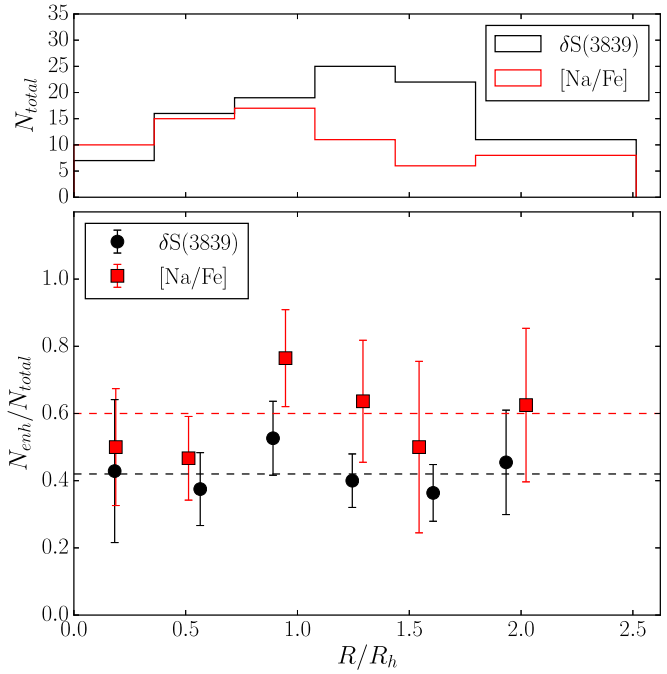

Figure 8. Top: A histogram of RGB stars as a function of radial distance from the cluster center in units of half-light radius where $R_h = 100.2''$ (Harris 1996 [2010 edition]). Our sample is shown in black, and RGB stars with a [Na/Fe] measurement from Sneden et al. (1994), Ramírez & Cohen (2002), Carretta et al. (2009a, 2009b), or Cordero et al. (2015) are combined into one sample shown in red. Bottom: The ratio of CN/Na-enhanced RGB stars to the total number of RGB stars in each radial bin from the top panel. Each point is at the average location of the stars in a given bin. The ratio calculated using the δS (3839) band to sort into populations is shown as black circles, and the ratio calculated using [Na/Fe] abundance is shown as red squares. Error bars are uncertainties based on Poisson statistics. A black dashed line is shown to indicate the ratio calculated for our entire sample. A red dashed line is shown to represent the approximate ratio determined using the Na abundances from the literature and [Na/Fe] = 0.3 dex (from Carretta et al. 2009a, 2009b) as a separating value.

material that forms the second generation of stars, the second generation should be enhanced in Na and depleted in O compared to the first (Gratton et al. 2012). The two main processes involved that create these anti-correlations (C–N and Na–O) are the CN(O)-cycle and the Ne–Na cycle. The C–N anti-correlation is a direct result of the CN(O)-cycle as it works in the progenitor stars to turn carbon into nitrogen. This carbon-depleted and nitrogen-enriched material is then ejected from the progenitor stars and enriches the intracluster medium, which then forms the second generation. The Na–O correlation is a result of both cycles working alongside each other. As the CN(O)-cycle causes a depletion in oxygen, the Ne–Na cycle converts neon to sodium in the same progenitor stars. Once again, this material is ejected from the progenitors and pollutes the intracluster medium, which the second population forms from. The second generation is therefore depleted in carbon and oxygen, and enhanced in nitrogen and sodium compared to the first.

This Na–O anti-correlation has been used frequently to identify multiple populations in GCs (see, e.g., Carretta et al. 2009a, 2009b; Gratton et al. 2012, and references therein). Multiple studies have looked at how N correlates with Na and O to see if these elements are classifying stars into the same populations (see, e.g., Smith et al. 2013; Smith 2015a, 2015b; Boberg et al. 2016, and references therein). Any outliers among these correlations could hint at stars with an interesting nucleosynthesis history and provide additional constraints for scenarios of multiple populations' formation. While most stars in the GCs studied fell into the same population regardless of whether CN band strength or Na abundance was used, a few stars in M5, 47 Tuc, and M53 have been found to have CN-enhanced band strengths without having enhanced Na abundances (Smith et al. 2013; Smith 2015a, 2015b; Boberg et al. 2016).

As we stated in Section 2.1, we prioritized observing stars with Na and O measurements in M71 to compare these two methods of identifying multiple populations with a large homogeneous sample. Final Na and O abundances for our stars come from Sneden et al. (1994), Ramírez & Cohen (2002), Carretta et al. (2009a, 2009b), and Cordero et al. (2015). Smith (2015b), in his analysis of M71, determined the small offsets in abundances measured from these sources (∼0.1 to 0.2 dex). We adopt the same offsets to put all samples cited above on the same standard scale for our study.

Since we have two CN band measurements for our stars in M71, we compare both of them to the Na and O abundances, which can be seen in Figure 9 where we have plotted [Na/Fe] and [O/Fe] versus δS(3839) and δCN(4216). Overall, we find that both of our δCN indices correlate with [Na/Fe] and anti-correlate with [O/Fe] as expected for RGB, AGB, and HB stars, even though the HB stars seem to have slightly lower Na and slightly higher O than the RGB stars in the sample. To better evaluate whether there are any CN-normal stars with enhanced Na or depleted O or vice versa, we have indicated the population of each star as classified by this work in Figure 9 by representing CN-enhanced stars as filled points and CN-normal stars as open. Once stars are coded in this way, Figure 9 shows that most stars fall in the correct place in the Na versus δCN and O versus δCN planes, save for a few exceptions. There is one HB star (ID = 153) that has been classified as CN-enhanced, but is found to have a [Na/Fe] value of ∼0.2 dex, which better matches the [Na/Fe] values of the CN-normal population. There is also one AGB star (ID = 102) that has very depleted O for a CN-normal star, but its [Na/Fe] value matches that of other CN-normal stars. As far as RGB stars that appear out of place, we identified two stars in Section 3.3 that were misidentified by their δS(3839) measurements, and both of these appear out of place in Figure 9.

The RGB star with ID = 63 (with δS(3839) = 0.008 and [Na/Fe] = 0.230) is one of the coolest stars in our sample ($T_{\rm eff}$ = 3810 K), which means it was misidentified due to the S(3839) band losing sensitivity faster than the CN(4216) band at cooler temperatures. This star was identified by the δS(3839) band as a CN-enhanced star, and it appears in the [Na/Fe] versus δS(3839) plot (top left panel of Figure 9) as one of the CN-enhanced stars with a low [Na/Fe] value. However, from the [Na/Fe] versus δCN(4216) plot and the [O/Fe] versus δCN (4216) (bottom left and right panels of Figure 9), it is clear that the star is misidentified by its δS(3839) as its [Na/Fe], [O/Fe], and δCN(4216) measurements all match the CN-normal population. Similarly, the other misidentified RGB star (ID = 99, δS(3839) = −0151, [Na/Fe] = 0.408), is a star that was identified as CN-normal, but from Figure 9, it appears to have a [Na/Fe] and δCN(4216) index measurement similar to the CN-enhanced population. Fortunately, these misidentifications by δS(3839) do not affect our calculations for the ratio of CN-enhanced to CN-normal stars in Section 4.1 because we have one misidentified star in each population. There are also

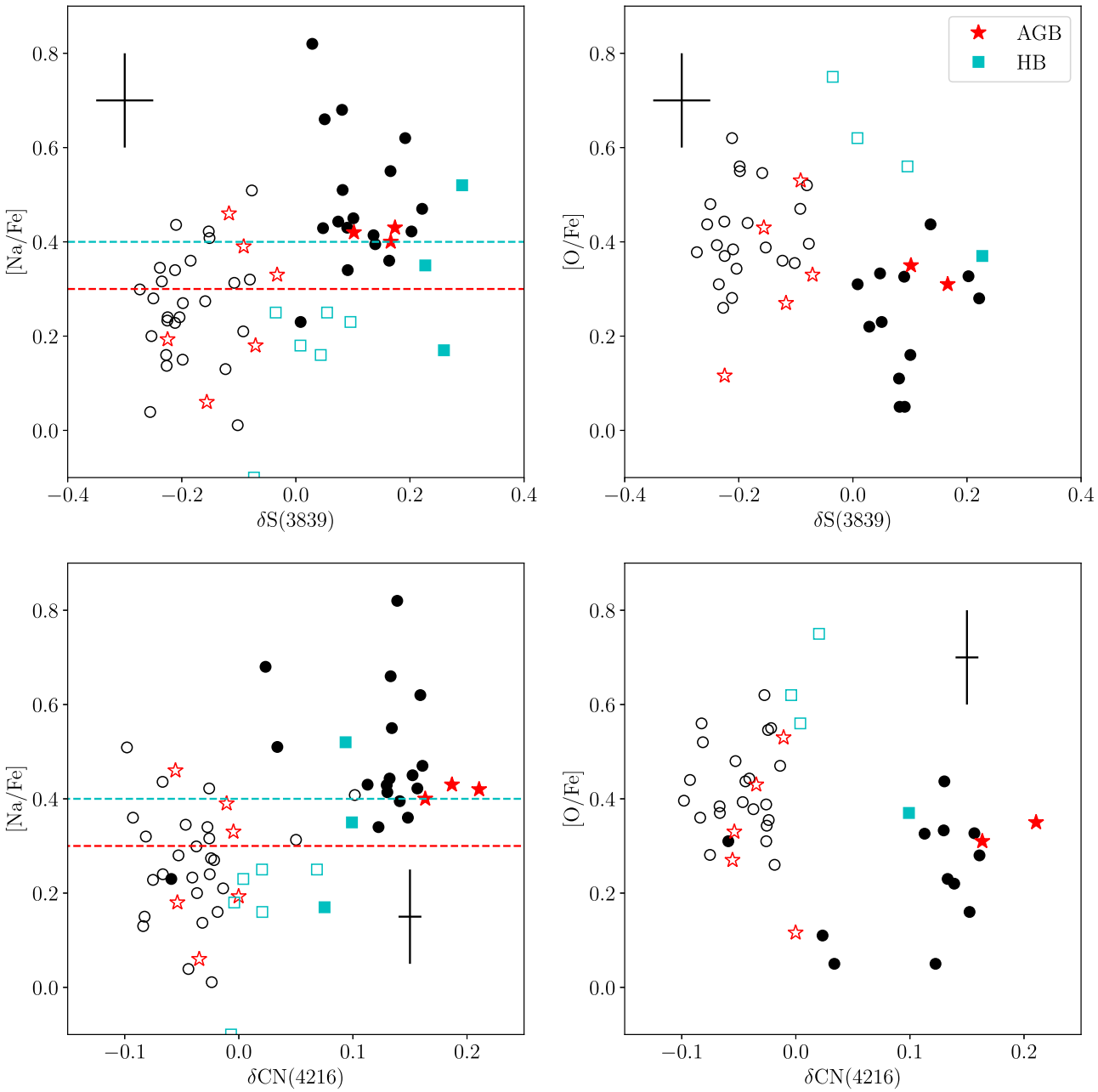

Figure 9. Top Left: [Na/Fe] versus δS(3839) for all stars in our sample with [Na/Fe] measurements. A red dashed line is placed where the division in populations is defined for [Na/Fe] (Carretta et al. 2009a, 2009b). A blue dashed line shows the separation in [Na/Fe] increased by 0.1 dex. Top Right: [O/Fe] versus δS(3839) for all stars in our sample with [O/Fe] measurements. Bottom Row: the same as the top row except for δCN(4216) instead of δS(3839). In all panels, symbols are coded as in Figure 1, CN-enhanced stars are filled, and CN-normal stars are open.

two CN-enhanced RGB stars with a δCN(4216) measurement close to 0.0 that have very low [O/Fe] measurements. These stars have lower δCN(4216) values than other CN-enhanced stars because they are two of the coolest stars in the sample ($T_{\rm eff} \leqslant 3900$), which means the CN(4216) band is not as sensitive to underlying changes in N abundance. They are likely still identified correctly as they have enhanced Na and depleted O as seen in Figure 9.

Finally, Figure 9 shows some RGB stars that are CN-normal, but fall above the [Na/Fe] = 0.3 dividing line used by Carretta et al. (2009a, 2009b) to denote the Na-enhanced population. We note that while the bimodal distribution of δCN leads to a relatively secure assignment to populations, the continuous nature of the [Na/Fe] distribution makes such a separation difficult. The identification of a single value of [Na/Fe] to classify different populations is likely to lead to the misclassification of a few stars near the chosen Na threshold. This can easily lead to some stars in each of the CN populations having slightly high or low Na values compared to the other stars in their population.

As Carretta et al. (2009a, 2009b) point out, the specific value of [Na/Fe] adopted in their analysis to separate the first and second generation stars is just indicative and not meant to provide a strict classification. We note that the CN-normal stars above the Na dividing line are at most only ~0.2 dex more enhanced than other CN-normal stars, and that they no longer seem out of place if the line separating the populations in [Na/Fe] is moved up just 0.1 dex to [Na/Fe] = 0.4 dex, which

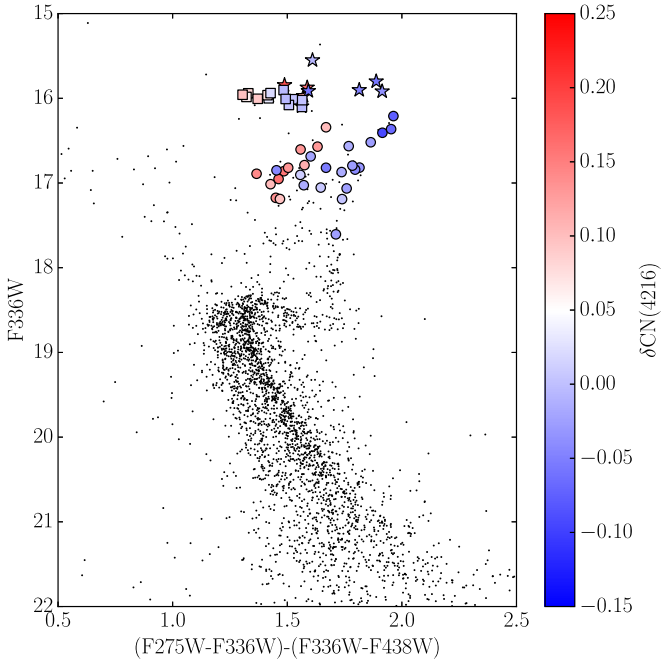

Figure 10. *HST* UV photometry for M71 using the pseudo-CMD as seen in Milone et al. (2017). Stars from our sample are indicated with RGB stars as circles, AGB stars as stars, and HB stars as squares. All stars in common with this study are color-coded based on δCN(4216) value.

is shown in the top and bottom left panels of Figure 9 as a blue dashed line. Setting the separation to [Na/Fe] = 0.4 dex also changes the percentage of stars identified to be second generation stars by Na abundance from 60% to 33%, which comes closer to the value we find based on our δCN strengths from Section 4.1 and that found by Bowman et al. (2017).

4.3.2. HST *UV Legacy Archive Photometry*

HST UV photometry has also been used in recent years to identify multiple populations in GCs based on a pseudocolor that is dependent on the C, N, and O abundances in a star (see Piotto et al. 2015; Milone et al. 2017). Designed as a way to increase the separation between the two populations seen in RGB's of the CMD of a cluster, this pseudocolor is made up of *HST* filters that are centered on NH, CH, OH, and CN bands. Since these bands are affected by C, N, and O abundances, which are different between the populations in GCs, the different populations separate themselves well enough in the pseudo-CMD to be identified with N-enhanced stars appearing on the "bluer" branch and N-normal stars appearing on the "redder" branch.

M71 was included in the *HST* UV Legacy Survey of Galactic GCs conducted by Milone et al. (2017), and this photometry is shown in Figure 10. M71 has a clear separation on the RGB into two populations, and Milone et al. (2017) find that 37.8% ± 3.8% of stars in the cluster belong to the second generation, in agreement with our findings based on δCN measurements.

In Figure 10 we also show stars in common between the *HST* photometry and our study, color-coded based on δCN(4216) strength. RGB stars are indicated as circles, AGB stars as stars, and HB stars as squares. For all three evolutionary stages of stars, CN-enhanced stars and CN-normal stars generally fall in the correct place on the pseudo-CMD with CN-enhanced stars being "bluer" than CN-normal stars. There is one RGB star that is CN-normal but sits on the "blue" CN-enhanced star sequence. A possible explanation for this is the relatively high amount of reddening seen toward the direction of this cluster compared to other GCs. This reddening would have a larger effect on the bluer photometric bands used for this analysis and has also been shown to change across the cluster (Morrison et al. 2016). Variable reddening could possibly cause a star to appear "redder" than it actually is. Even with this one outlier, we are left with the result that the *HST* UV photometry method and our δCN method of identifying multiple populations are classifying stars into the same populations in general, which agrees with what we found in M10 (G18).

5. Conclusions

We have classified 100 RGB, 15 AGB, and 27 HB stars in M71 into CN-enhanced and CN-normal populations based on CN band measurements made with low-resolution spectroscopy. We then calculate the ratio of first and second generation stars in each evolutionary stage, find the He abundance difference between the populations, study the radial distribution of each population, and compare our methods of classification to others used in the literature to identify multiple populations in GCs. Our conclusions based on this analysis are listed below:

1. We classify stars into populations based on both the S(3839) and CN(4216) CN band indices measured for this cluster. For the brighter, cooler stars ($M_V \leqslant 3.0$, $T_{\rm eff} \leqslant 5300$ K), the separation in the CN(4216) band strength can be clearly seen by eye. We create a δS(3839) and δCN(4216) index and fit both distributions with GMMs. These models indicate that two populations are needed to best explain the distribution of both δCN indices. We find that unlike most clusters, which are dominated by the CN-enhanced population (see, e.g., Milone et al. 2017), M71 is a CN-normal, first generation dominated cluster with 58% ± 4% of RGB stars belonging to the first generation.
2. We determine a C and N abundance for each population based on matching δS(3839) and δCN(4216) indices versus effective temperature with models generated with the SSG. The CN-enhanced population is best fit with [C/Fe] = −0.3 dex and [N/Fe] = 1.5 dex, and the CN-normal population is best fit with [C/Fe] = 0.0 dex and [N/Fe] = 0.6 dex. These results agree well with what was found for giant stars from DDO photometry by Briley et al. (2001b) and with C and N abundances measured for main sequence stars by Briley & Cohen (2001a) and Briley et al. (2004). The separation in [N/Fe] between the two populations of 0.9 dex is comparable to the 0.7 dex separation found in M10 (G18).
3. The AGB and HB stars in M71 separate into two populations with a similar ratio between CN-enhanced and CN-normal stars as the RGB stars. This means that both generations of stars are moving onto the HB and AGB. Furthermore, the HB stars' location on the CMD seems to be dependent on CN band strength with the average position of the CN-enhanced stars on the HB being brighter than the average position of the CN-normal stars by 0.08 magnitudes. This result is consistent with what is seen in 47 Tuc, a cluster of similar

metallicity (Briley 1997). Through ZAHB fitting using PGPUC isochrones, we determine that this difference in HB position is consistent with the CN-enhanced stars having a Y value higher by 0.025. This ΔY is consistent with what is found by Milone et al. (2018) using *HST* UV photometry.

4. We find that the fraction of CN-enhanced stars does not vary with the distance from the cluster's center. The same result is found when [Na/Fe] is used to classify stars. M71 is a dynamically old cluster, and the complete spatial mixing of the two populations observed is consistent with being the result of dynamical evolution.
5. Based on stars in our sample with Na and O measurements (Sneden et al. 1994; Ramírez & Cohen 2002; Carretta et al. 2009a, 2009b; Cordero et al. 2015) and those with *HST* UV photometry (Milone et al. 2017), we find no major discrepancies between any of the different methods of classifying multiple populations in M71. While the HB stars seem to have slightly lower Na abundances than the RGB stars, they still correlate with δCN strength as expected. There is a group of stars that appears to be CN-normal with slightly enhanced Na based on the definition separating populations from Carretta et al. (2009a, 2009b) of [Na/Fe] = 0.3 dex, but if the separating value is raised by only 0.1 dex to [Na/Fe] = 0.4 dex, then this group no longer exists. Raising the separating value also brings the ratio of second generation stars from 60% to 33%, which comes closer to agreement with the ratio we find using δCN, the ratio found by Milone et al. (2017) with *HST* photometry, and the ratio found by Bowman et al. (2017) with narrow, CN-band photometry. Additionally with the exception of one HB star, we do not observe any CN-enhanced stars with normal [Na/Fe] values as reported by Smith et al. (2013), Smith (2015a), and Boberg et al. (2016) in M5, 47 Tuc, and M53, respectively.

We would like to thank Roger A. Bell for making the SSG program available to us, and Kyle Cudworth for sharing his M71 proper motions and membership probabilities. We would also like to thank Zachary Maas for his help in obtaining the stellar spectra during our 2016 run at WIYN. Additionally, we would like to thank Dianne Harmer, Daryl Willmarth, and all of the observing assistants who helped with our multiple runs on Hydra.

This publication makes use of data products from the Two Micron All Sky Survey, which is a joint project of the University of Massachusetts and the Infrared Processing and Analysis Center/California Institute of Technology, funded by the National Aeronautics and Space Administration and the National Science Foundation.

ORCID iDs

Jeffrey M. Gerber https://orcid.org/0000-0001-9583-0004
Enrico Vesperini https://orcid.org/0000-0003-2742-6872

References

Alonso, A., Arribas, S., & Martínez-Roger, C. 1999, A&AS, 140, 261
Alonso, A., Arribas, S., & Martínez-Roger, C. 2001, A&A, 376, 1039
Baumgardt, H., & Makino, J. 2003, MNRAS, 340, 227
Bekki, K. 2010, ApJL, 724, L99
Bell, R. A., Paltoglou, G., & Tripicco, M. J. 1994, MNRAS, 268, 771
Bellini, A., Piotto, G., Bedin, L. R., et al. 2009, A&A, 507, 1393
Boberg, O. M., Friel, E. D., & Vesperini, E. 2016, ApJ, 824, 5
Bowman, W. P., Pilachowski, C. A., van Zee, L., et al. 2017, AJ, 154, 131
Brasseur, C. M., Stetson, P. B., VandenBerg, D. A., et al. 2010, AJ, 140, 1672
Briley, M. M. 1997, AJ, 114, 1051
Briley, M. M., & Cohen, J. G. 2001a, AJ, 122, 242
Briley, M. M., Harbeck, D., Smith, G. H., & Grebel, E. K. 2004, AJ, 127, 1588
Briley, M. M., Smith, G. H., & Claver, C. F. 2001b, AJ, 122, 2561
Brown, J. M., Garaud, P., & Stellmach, S. 2013, ApJ, 768, 34
Campbell, S. W., D'Orazi, V., Yong, D., et al. 2013, Natur, 498, 198
Campbell, S. W., Yong, D., Wylie-de Boer, E. C., et al. 2012, in ASP Conf. Ser. 458, Galactic Archaeology: Near-field Cosmology and the Formation of the Milky Way, ed. W. Aoki, M. Ishigaki, & T. Suda (San Fransisco, CA: ASP), 205
Carretta, E. 2015, ApJ, 810, 148
Carretta, E., Bragaglia, A., Gratton, R., & Lucatello, S. 2009a, A&A, 505, 139
Carretta, E., Bragaglia, A., Gratton, R. G., et al. 2009b, A&A, 505, 117
Carretta, E., Bragaglia, A., Gratton, R. G., et al. 2010, A&A, 516, A55
Charbonnel, C., & Zahn, J.-P. 2007, A&A, 467, L15
Cohen, J. G., Behr, B. B., & Briley, M. M. 2001, AJ, 122, 1420
Cordero, M. J., Pilachowski, C. A., Johnson, C. I., & Vesperini, E. 2015, ApJ, 800, 3
Cudworth, K. M. 1985, AJ, 90, 65
Dalessandro, E., Cadelano, M., Vesperini, E., et al. 2019, ApJL, 884, L24
Dalessandro, E., Massari, D., Bellazzini, M., et al. 2014, ApJL, 791, L4
D'Antona, F., Vesperini, E., D'Ercole, A., et al. 2016, MNRAS, 458, 2122
D'Ercole, A., D'Antona, F., Carini, R., et al. 2012, MNRAS, 423, 1521
D'Ercole, A., Vesperini, E., D'Antona, F., McMillan, S. L. W., & Recchi, S. 2008, MNRAS, 391, 825
De Marchi, G., Paresce, F., & Pulone, L. 2007, ApJL, 656, L65
de Mink, S. E., Pols, O. R., Langer, N., et al. 2009, A&A, 507, L1
Decressin, T., Charbonnel, C., & Meynet, G. 2007a, A&A, 475, 859
Decressin, T., Meynet, G., Charbonnel, C., et al. 2007b, A&A, 464, 1029
Denissenkov, P. A., & Hartwick, F. D. A. 2014, MNRAS, 437, L21
Denissenkov, P. A., & Merryfield, W. J. 2011, ApJL, 727, L8
Di Cecco, A., Bono, G., Prada Moroni, P. G., et al. 2015, AJ, 150, 51
Dinescu, D. I., Girard, T. M., & van Altena, W. F. 1999, AJ, 117, 1792
Eggleton, P. P., Dearborn, D. S. P., & Lattanzio, J. C. 2006, Sci, 314, 1580
Elmegreen, B. G. 2017, ApJ, 836, 80
Elsner, R. F., Heinke, C. O., Cohn, H. N., et al. 2008, ApJ, 687, 1019
Friel, E. D. 1987, AJ, 93, 1388
García-Hernández, D. A., Mészáros, S., Monelli, M., et al. 2015, ApJL, 815, L4
Gerber, J. M., Friel, E. D., & Vesperini, E. 2018, AJ, 156, 6
Gieles, M., Charbonnel, C., Krause, M. G. H., et al. 2018, MNRAS, 478, 2461
Gratton, R. G., Carretta, E., & Bragaglia, A. 2012, A&ARv, 20, 50
Grundahl, F., Stetson, P. B., & Andersen, M. I. 2002, A&A, 395, 481
Gustafsson, B., Edvardsson, B., Eriksson, K., et al. 2008, A&A, 486, 951
Harbeck, D., Smith, G. H., & Grebel, E. K. 2003, AJ, 125, 197
Harris, W. E. 1996, AJ, 112, 1487
Helmi, A., Babusiaux, C., Koppelman, H. H., et al. 2018, Natur, 563, 85
Henkel, K., Karakas, A. I., & Lattanzio, J. C. 2017, MNRAS, 469, 4600
Johnson, C. I., Kraft, R. P., Pilachowski, C. A., et al. 2005, PASP, 117, 1308
Johnson, C. I., McDonald, I., Pilachowski, C. A., et al. 2015, AJ, 149, 71
Johnson, C. I., & Pilachowski, C. A. 2012, ApJL, 754, L38
Keller, L. D., Pilachowski, C. A., & Sneden, C. 2001, AJ, 122, 2554
Kimmig, B., Seth, A., Ivans, I. I., et al. 2015, AJ, 149, 53
Kippenhahn, R., Ruschenplatt, G., & Thomas, H.-C. 1980, A&A, 91, 175
Kirby, E. N., Guo, M., Zhang, A. J., et al. 2015, ApJ, 801, 125
Kraft, R. P. 1994, PASP, 106, 553
Lagioia, E. P., Milone, A. P., Marino, A. F., et al. 2018, MNRAS, 475, 4088
Lardo, C., Bellazzini, M., Pancino, E., et al. 2011, A&A, 525, A114
MacLean, B. T., Campbell, S. W., De Silva, G. M., et al. 2016, MNRAS, 460, L69
MacLean, B. T., Campbell, S. W., De Silva, G. M., et al. 2018, MNRAS, 475, 257
Marigo, P., Girardi, L., Bressan, A., et al. 2017, ApJ, 835, 77
Miholics, M., Webb, J. J., & Sills, A. 2015, MNRAS, 454, 2166
Milone, A. P., Marino, A. F., Piotto, G., et al. 2015a, ApJ, 808, 51
Milone, A. P., Marino, A. F., Piotto, G., et al. 2015b, MNRAS, 447, 927
Milone, A. P., Marino, A. F., Renzini, A., et al. 2018, MNRAS, 481, 5098
Milone, A. P., Piotto, G., Bedin, L. R., et al. 2012, ApJ, 744, 58
Milone, A. P., Piotto, G., Renzini, A., et al. 2017, MNRAS, 464, 3636
Morrison, H. L., Ma, Z., Clem, J. L., et al. 2016, AJ, 151, 7
Nardiello, D., Milone, A. P., Piotto, G., et al. 2015, A&A, 573, A70

Norris, J., & Freeman, K. C. 1979, ApJL, 230, L179
Peterson, R. C., & Latham, D. W. 1986, ApJ, 305, 645
Piotto, G., Milone, A. P., Bedin, L. R., et al. 2015, AJ, 149, 91
Prantzos, N., & Charbonnel, C. 2006, A&A, 458, 135
Ramírez, S. V., & Cohen, J. G. 2002, AJ, 123, 3277
Simioni, M., Milone, A. P., Bedin, L. R., et al. 2016, MNRAS, 463, 449
Simpson, J. D., Martell, S. L., & Navin, C. A. 2017, MNRAS, 465, 1123
Skrutskie, M. F., Cutri, R. M., Stiening, R., et al. 2006, AJ, 131, 1163
Smith, G. H. 2015a, PASP, 127, 825
Smith, G. H. 2015b, PASP, 127, 1204
Smith, G. H., Modi, P. N., & Hamren, K. 2013, PASP, 125, 1287
Smith, G. H., Shetrone, M. D., & Strader, J. 2007, PASP, 119, 722
Sneden, C., Kraft, R. P., Langer, G. E., Prosser, C. F., & Shetrone, M. D. 1994, AJ, 107, 1773
Traxler, A., Garaud, P., & Stellmach, S. 2011, ApJL, 728, L29
Valcarce, A. A. R., Catelan, M., & De Medeiros, J. R. 2013, A&A, 553, A62
Valcarce, A. A. R., Catelan, M., & Sweigart, A. V. 2012, A&A, 547, A5
Ventura, P., D'Antona, F., Mazzitelli, I., et al. 2001, ApJL, 550, L65
Vesperini, E., & Heggie, D. C. 1997, MNRAS, 289, 898
Vesperini, E., McMillan, S. L. W., D'Antona, F., & D'Ercole, A. 2013, MNRAS, 429, 1913
Wachlin, F. C., Miller Bertolami, M. M., & Althaus, L. G. 2011, A&A, 533, A139